THE JOURNAL OF PHYSICAL CHEMISTRY C

Article

Cite This: J. Phys. Chem. C 2018, 122, 18012−18020

pubs.acs.org/JPCC

Control of Electric Field Localization by Three-Dimensional Bowtie Nanoantennae

Ari D. Mayevsky and Alison M. Funston*

ARC Centre of Excellence in Exciton Science and School of Chemistry, Monash University, Clayton 3800, Australia

Supporting Information

ABSTRACT: The three-dimensional morphological control of the individual metallic nanocrystals in a coupled structure imposes an electric field localization and enhancement in all three dimensions. We exploit the unique morphology of chemically synthesized nanotriangle monomers to form assembled dimers with a bowtie-like morphology in two orthogonal planes, effectively minimizing the volume of the interaction space to a point. The antenna has a longitudinal mode at 893 nm (1.39 eV), a 294 nm (0.68 eV) red shift compared to a monomer of equivalent size. This is indicative of extremely strong coupling because of the three-dimensional confinement of the electric field within the nanogap. By changing the geometry of the nanotriangle dimer, the longitudinal mode is tunable within a 220 nm (0.45 eV) range. The distribution of the electric field in the interparticle space transitions from a localized point for a bowtie to a more distributed line for an inverted bowtie.

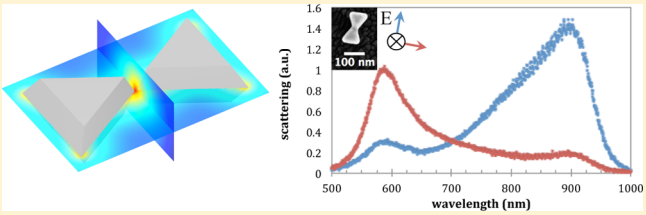

INTRODUCTION

The ability to manipulate light on the nanoscale is an intrinsic consequence of the optical response of metal nanoparticles. The spatial confinement of conduction electrons in sub-wavelength structures such as metal nanocrystals leads to localized surface plasmon resonances (LSPRs) and a concomitant enhancement of the electromagnetic field close to the nanoparticle surface (near field), that is, on the nanoscale.[1] The nanoparticle shape and size dramatically influence the location, physical extent, and intensity of the confined field as well as the resonance energy.[2] As a plasmon resonance is an electron cloud oscillation, the resonance modulates the charge distribution over the nanoparticle with time. Thus, the plasmon resonances of two nanoparticles in close proximity interact to create localized areas of extremely high field enhancement.[2] This provides a means for increasing the sensitivity within chemical and biological sensing applications, including surface-enhanced Raman scattering and LSPR sensing, as well as optoelectronic applications.[1]

Nanostructures with three-dimensional morphology give the possibility for three-dimensional tuning of the electric field enhancement either into specific areas or much more tightly confined volumes.[3] The targeted assembly of these nanostructures allows further manipulation of the electric field spatial distribution, extent, and magnitude. However, nanoparticles fabricated using physical methods such as electron beam lithography are subject to a number of fine structural aberrations such as polycrystallinity, vertex rounding, and surface roughness.[4,5] As a result, these structures tend to have poorer optical properties than an equivalent crystalline structure.[6] Also, such fabrication procedures only have limited control over z-dimension morphology, complicating the engineering of the volume of interaction space. Colloidally synthesized metal nanoparticles are crystalline with minimal surface roughness, providing a means of avoiding features that cause such optical losses. Additionally, nanocrystals with features like sharp vertices, such as nanotriangles[7] and nanostars,[8] can be synthesized, affording the means of increasing electric fields within monomer nanoparticles,[3] and their assembly into dimers has been shown to improve this further.[2,9−11] An additional advantage of directed self-assembly methods is the ability to achieve the very small interparticle separations, of the order of 1 nm,[10,12−15] required for the highest electric field enhancement.[16]

The electric field interaction between nanoparticles has been described using the electromagnetic analogue of molecular orbital theory, the plasmon hybridization model.[2,17,18] This coupling leads to a polarization-dependent splitting of the plasmon resonance.[19] For polarization of the electric field along the interparticle axis, an attractive interaction results in the stabilization of the resonance which requires less energy for excitation. This causes the mode to red-shift relative to that of the uncoupled particle. Polarization perpendicular to the interparticle axis leads to a higher energy, repulsive interaction, and a blue shift of the plasmon resonance is observed.[2,10,17,18,20] These plasmon resonance shifts typically increase as the interparticle spacing is reduced,[19] but large shifts can also be seen in fundamentally highly efficiently coupled structures.[2,10,21] Simulations have shown that coupling strength correlates with electric field enhancement and

Received: June 18, 2018
Revised: July 13, 2018
Published: July 30, 2018

DOI: 10.1021/acs.jpcc.8b05805
J. Phys. Chem. C 2018, 122, 18012−18020

localization[11] and that the greatest electric field enhancements should occur in structures with minimal interparticle separation outside of the electron tunneling range.[16,22]

Bowtie nanoantennae, which consist of two triangular nanoparticles aligned in a tip-to-tip fashion, have been proposed as ideal structures to produce highly localized and enhanced electric fields in the interparticle space because of the confinement of the extent of the interaction space by the low radius of curvature of the triangle vertices.[23] Dimers which are precisely aligned are predicted to focus the electric field, causing enhancements of up to 3 orders of magnitude.[9,13,23−25] Systematic studies of the optical properties for these structures have shown that, in accordance with numerical simulations, reductions in interparticle separation produce greater plasmon band splitting and increases in longitudinal resonance mode cross section,[9,26] and increasing the size of the nanotriangles in these structures produces overall spectral red shifts.[9,26,27] Rotation[28] and truncation[29] can also lead to changes in the optical spectra. In both experiments and in simulations, the nanoparticles are shaped like triangular prisms, and therefore the field enhancement manifests as a line that extends across the thickness of the prisms.[23,25] Simulations have suggested that reducing the prism thickness (nanoparticle z-dimension) could enhance and localize the electric field.[23] This has significant implications when considering that reduction in thickness provides a means of enhancement by confinement in the z-dimension; however, this notably changes the volume of the nanoparticles and has obvious limitations.

An alternative means of confinement is applying the reduction in the radius of curvature in the z-dimension, potentially circumventing this limitation. In effect, this functions by sharpening the prism edge to a point, minimizing the height of the interaction space. This three-dimensional structure is achievable through chemical synthesis, and as a result, the assembly of these particles into an ideal dimer forms a bowtie not only in the $x-y$ substrate plane, but also in the $y-z$ cross section. A bowtie nanoantenna composed of such nanoparticles is therefore a highly promising system to enable three-dimensional electric field confinement, and, consequently, strong enhancement in the interparticle space.

We report the DNA-directed assembly[14,30−35] of such chemically grown, crystalline, triangular nanoparticles into dimers. The scattering spectra of dimers across a range of geometries were collected via dark-field microscopy. The geometries included a bowtie antenna as well as a series of triangle dimers aligned along their edges. We show the manipulation of the electric field in three dimensions as a function of the geometry of the nanocrystalline dimer.

METHODS

Materials. $HAuCl_4 \cdot 3H_2O$ (≥99.9%), $NaBH_4$ (Reagent Plus, 99%), polyvinylpyrrolidone (PVP) ($M_w \approx 10\,000$ $gmol^{-1}$) (PVP10), PVP ($M_w \approx 40\,000$ $gmol^{-1}$) (PVP40), and (3-mercaptopropyl)trimethoxysilane (MPTES, 95%) were purchased from Sigma-Aldrich. Ethanol (96%), isopropanol (Analysis, ACS, ISO), *N*,*N*-dimethylformamide (DMF), and toluene (GR) were purchased from Merck. Tris(2-carboxyethyl)phosphine hydrochloride (98%) (TCEP) was purchased from Acros. Thiol-terminated oligonucleotides were obtained from Geneworx. Water used was of Milli-Q grade. All chemicals were used as received.

Instrumentation. Ultrasonic irradiation was performed using a Sonics & Materials Vibra Cell VC600 ultrasonic processor (5 mm tip radius) operating at a frequency of 20 kHz with the amplitude set to 5. Scanning electron microscopy (SEM) images were obtained with an FEI Nova NanoSEM 450 or an FEI Helios 600 D545 SEM. Location markers were milled on the slides using a gallium ion focused ion beam (FIB) attached to the FEI Helios 600 D545 SEM. The absorbance spectra were measured using a Cary 60 UV−vis spectrophotometer (Agilent Technologies).

Gold Nanoparticle Synthesis. Gold nanotriangles were synthesized according to the methods reported by Sánchez-Iglesias et al.[7] Briefly, seed particles were synthesized by the addition of an aqueous $HAuCl_4$ solution (5 μL, 0.05 M) to a PVP10 solution in DMF (4.5 mL, 40 μM). An aqueous solution of $NaBH_4$ (245 μL, 10 mM) was injected quickly into the seed growth solution under vigorous stirring. The mixture was stirred for 2 h at room temperature. The seeds were then allowed to rest for 24 h before use.

An overgrowth solution of PVP40 in DMF (4.5 mL, 2.5 mM) was heated to 100 °C and an aqueous solution of $HAuCl_4$ (250 μL, 0.05 M) was added over 2 min. The resultant solution was stirred at 100 °C for 1 h and 55 min. Then, 0.1 mL of the previously formed seed solution was added, and the mixture was ultrasonically irradiated until the completion of the reaction, indicated by no further red shift of the maximum absorbance peak.

Upon completion of the reaction, the resultant nanoparticles were cleaned by centrifugation of the dispersion, removal of 90% of the supernatant, followed by resuspension in an equivalent volume of ethanol. The centrifugation and resuspension were repeated twice.

A UV−visible spectrum for the colloid is shown in Figure S1.

Sample Preparation. Indium tin oxide (ITO)-coated slides were cleaned by sequential sonication in isopropanol and then water for 20 min each. The slides were thoroughly rinsed with water and dried completely under a stream of nitrogen. The slide surface was functionalized using MPTES. A clean, dry slide was added to a solution of MPTES in toluene (5 mL, 0.056 M) at 60 °C and allowed to react for 4 min. The slide was removed from the solution, rinsed with toluene, and dried under nitrogen.

DNA Assembly and Deposition. The DNA-directed assembly of gold nanoparticles was performed using the procedures previously reported.[12,14,35] The oligonucleotides were thiolated at the 5′-terminal, and the strand sequences used were as follows: S1 = 5′-TGCAATCCTGAGCACA-3′ and S2 = 5′-TGTGCTCAGGATTGCA-3′. Prior to assembly, the aqueous oligonucleotide solution (2.5 μL, 100 mM) was reduced by incubation in a freshly prepared aqueous TCEP solution (22.5 μL, 0.2 mM) for 2 h. To bind the DNA to gold nanoparticles, the reduced oligonucleotide solution was added to a 100 μL aliquot of the cleaned nanotriangle ensemble solution, which was then left for 30 min for the functionalization to occur. The assembly of dimers was performed by the addition of a 125 μL aliquot of each of S1- and S2-functionalized nanoparticles into a reaction vessel, and the assembly was initiated by the addition of 4 mL of phosphate-buffered saline (0.01 M Na_2HPO_4, 0.0018 M KH_2PO_4, 0.137 M NaCl, and 0.0027 M KCl, pH 7.4). The assembly was continued for 10 s, and following this, the assembled structures were deposited on a glass substrate by dipping the MPTES-functionalized ITO slide into the assembly solution for 10 s and then immediately immersing

DOI: 10.1021/acs.jpcc.8b05805
J. Phys. Chem. C 2018, 122, 18012−18020

the slide in Milli-Q water for 30 min. The sample was then rinsed and dried in air. No significant structural modification of the deposited assemblies was observed over a 2-year period (Supporting Information, Figure S2).

The assembly time was restricted to ensure the minimal formation of larger aggregates. After 10 s of assembly, monomers remained the predominant product. The yield of dimers and higher order structures was 2.6 and 0.7%, respectively (total 3.4%), after this time. In contrast, using noncomplementary DNA resulted in only 0.5% dimers and higher-order structures. The colloid contains decahedra as its major shape product, and the majority of dimers and higher-order structures also necessarily contained decahedra. The yield of relevant nanotriangle dimers was thus <0.1%.

The dispersion in which DNA hybridization is carried out contains <5% ethanol. During the deposition and washing of the assemblies, the DNA is likely unhybridized; however, the particles remain in van der Waals contact, and so the conformation of the DNA strands does not influence the interparticle separation.

Dark-Field Microscopy. The scattering spectra of single nanostructures were collected on a dark-field microscope with a 100 W halogen lamp illumination source, a dark-field condenser (0.8−0.95 numerical aperture), and a Nikon Plan Fluor ELWD 40×/0.60 NA air objective. The collected light was focused onto the entrance slit of a MicroSpec 2156i imaging spectrometer coupled to a TE-cooled charge-coupled device (CCD) (Acton Pixis 1024B Excelon). The polarized scattering spectra were collected by rotating a polarizer (LPVIS 100, Thorlabs) in the light path just after the light source. All spectra were collected on ITO-coated glass microscope slides in air. A total of 21 spectra were collected per structure with the polarized irradiating light being rotated through 0−180° in increments of 10°, and an unpolarized spectrum was collected before and after. The spectra obtained were correlated with the electron micrographs of the structure using a FIB mark registration as a correlation marker, as reported by Novo et al.[36]

Data Analysis. The spectra were deconvolved by globally fitting across the polarized spectra of a given nanostructure. Individual spectral features were assumed to be Lorentzian, as such energy and peak width (full width at half-maximum) were treated as global variables. Although y-offset was not treated as a global variable, all Lorentzian contributions to a given spectrum were required to have the same y-offset value (i.e., one baseline value per spectrum). This allows the area and y-offset to vary with respect to the polarization state. All nanostructures were treated as the sum of one to three Lorentzian functions, determined individually according to the number of spectral contributions.

Numerical Simulations. The scattering cross sections of single nanoparticles and dimers were modeled using the discrete dipole approximation (DDA). DDA calculates the absorption and scattering cross sections of nanostructures using a shape approximation based on a volume discretization to create an array of cubic dipoles.[37] For these calculations, the program DDSCAT 7.1[37,38] was used to calculate the polarization of each dipole that results from the interaction with the irradiating field and the surrounding dipoles. The dielectric data of Weaver[39] were used, and the environment was set to a refractive index of 1.25 to simulate the experimental conditions.[40,41] For accuracy >5%, it is required that the interdipole spacing be small with respect to the frequency of the incoming radiation and particle size, specifically that $|m|kd < 0.05$. Hence, for these calculations, >100 000 dipoles were used for particles with a side length of 80 nm and an aspect ratio of 2:1 (edge length to thickness). The electric field of the incident light was polarized both along and perpendicular to the interparticle axis.

Scheme 1. Schematic Representation of Calculations for the Edge−Edge Offset in a Triangle Dimer

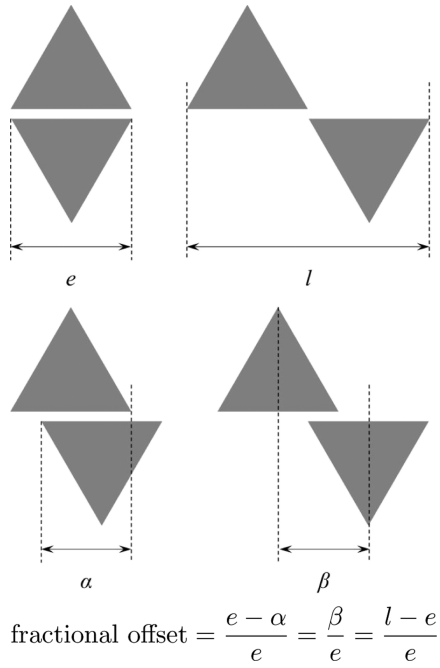

Offset for Nanotriangle Dimers. We report the structural details of the nanotriangle dimers in terms of their relative degree of offset. A schematic diagram for the measurement of the edge−edge offset of the nanotriangle dimers is shown in Scheme 1. In this case, e represents the average nanotriangle edge length in the dimer, α represents the overlap, β represents the center−center distance, and l represents the total length of the dimer. α, β, and l are all measured along the edge−edge axis, which is defined as the axis through the interparticle space that runs parallel to one side of each triangle in the dimer (i.e., horizontal for all structures in Scheme 1). An ideal inverted bowtie has an offset of 0% and an ideal bowtie will have an offset of 100%, with the latter varying with the interparticle separation.

The offset percentages are calculated from both α and β, and the listed offsets are the average of these values. There is no more than 6% difference between these two values for the experimental data presented in this work.

RESULTS AND DISCUSSION

Gold nanotriangles with a unique three-dimensional nanostructure, described as a truncated triangular bipyramid and shown in Figure 1, were synthesized according to the methods reported by Sánchez-Iglesias et al.[7] The nanotriangles were present in a 42% shape yield, and decadehra in 47% yield. Minor by-products included octahedra, bipyramids, and hexagonal plates. When viewed from the sides, the nanotriangles have an elongated hexagonal profile (Figure 1c,f), with the central, outermost triangular edges forming sharp vertices within the central plane (x−y plane illustrated by

DOI: 10.1021/acs.jpcc.8b05805
J. Phys. Chem. C 2018, 122, 18012−18020

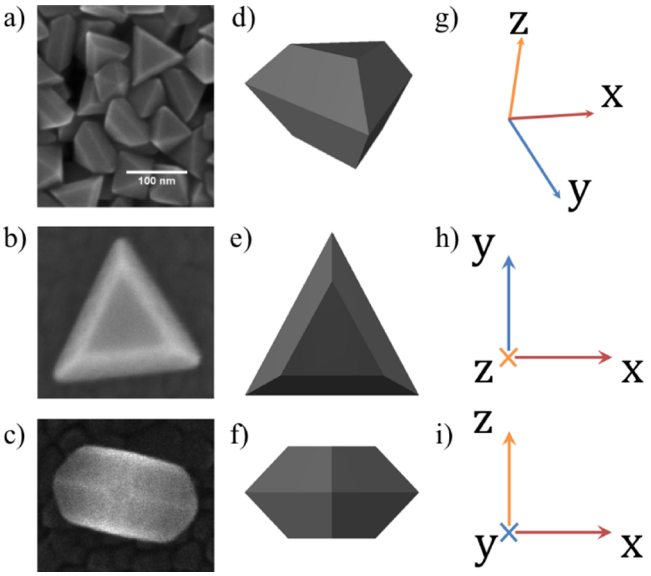

Figure 1. (a–c) SEM images of the (a) nanotriangle colloid, (b) a nanotriangle lying on its face, and (c) a nanotriangle standing on its edge. (d–f) Schematic representations of nanotriangle morphology. (g–i) Axes representing the orientations of the nanotriangles in (d–f).

Figure 1). The nanoparticles are crystalline with flat facets and a radius of curvature at the outermost tips of 4–5 nm. Although synthetic procedures for nanotriangles and triangular plates with high shape yield have been reported, these produce nanoparticles that have either notable asymmetry in the *z*-dimension[42] (nanotriangles) or lack the three-dimensional nanostructure[43] (plates) that was important for this work.

The assembly of the nanocrystals with the DNA-based approach used here formed dimers in a bowtie arrangement, as well as various other geometries. Higher-order structures were also observed. We note that the assembly is halted 10 s after the addition of salt via deposition of the structures onto the MPTES-functionalized substrate. MPTES assists in the retention of the assembly structure under the capillary forces experienced during drying of the sample. The selection of the structures of interest, that is, well-aligned nanotriangle dimers, is necessary via the FIB registration method.[36]

The nanoparticles are stabilized by a PVP ligand shell. The removal of this ligand becomes increasingly difficult with additional washing steps, and enough ligand is retained to maintain the colloidal stability of the nanoparticles even after extensive washing.[44] The PVP coating varies in thickness down to 0.5 nm, with a dependence on the radius of curvature,[45,46] because of the preferential adsorption of PVP to gold {111} facets and steric hindrance.[47] Therefore, the most likely site of DNA attachment is at a vertex, followed by an edge, followed by a facet. For these short DNA strands and larger particles, DNA hybridization and the subsequent deposition of the nanocrystals lead to the nanoparticles being in primary ligand contact,[14] likely with some ligand shell compression. The assembled nanostructures prepared by this method then have an interparticle distance of the order of ≤1.5 nm.[10,12−15,31,48] We note that SEM is a surface technique, and as such the ligand shell can be observed in the SEM images of the nanoantennae. This is most obvious in the interparticle space and has the effect of blurring the particle structural detail (as it is covered by a polymer), resulting in an apparent overlap of the nanocrystals; however this involves the contact of the polymer shell only, and not the metal nanoparticles. The ligand shell prevents the nanoparticles from reaching conductive contact, and no evidence of optical features characteristic of conductive contact[4,11,49] were observed.

The scattering spectra of single nanotriangles and their assemblies were determined using dark-field microscopy. The excitation light was formed into a hollow cone of light and focused on the sample with a dark-field condenser (0.8–0.95 NA). The scattered light from the single crystals/assemblies was collected with a Nikon Plan Fluor ELWD 40×/0.60 NA objective and focused onto the entrance slit of a MicroSpec 2156i coupled to a CCD (Acton Pixis 1024B Excelon). The polarized scattering spectra were collected by rotating a polarizer (LPVIS 100, Thorlabs) in the light path just after the light source.

The scattering spectra of single monomer nanotriangles with edge lengths of 90 and 75 nm are shown in Figure S3. Each of these have a single resonance, located at 610 nm (2.03 eV) and 599 nm (2.07 eV), respectively, and display little polarization

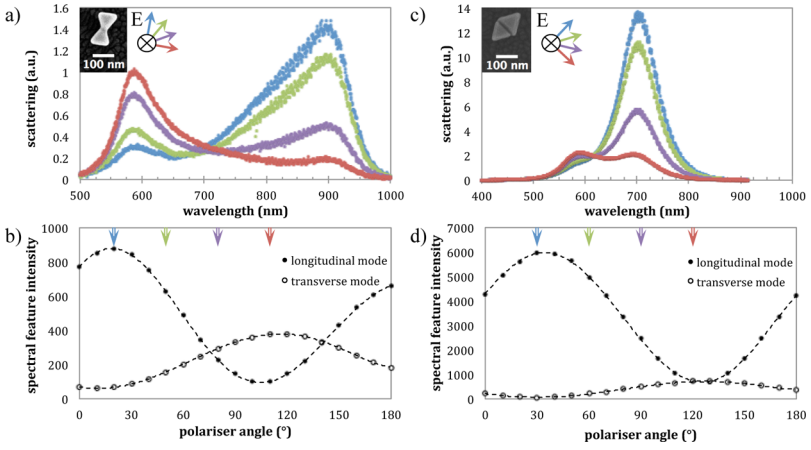

Figure 2. (a,c) Scattering spectra of (a) a bowtie nanoantenna and (c) an inverted bowtie (SEM images inset). The polarization of the irradiating light is represented by the arrows beside the SEM images. (b,d) Area of the longitudinal and transverse resonances as a function of excitation polarization for (b) the bowtie nanoantenna shown in (a), and (d) inverted bowtie shown in (c). The colored arrows in (b,d) represent the polarization angles of the scattering spectra shown in (a,b).

DOI: 10.1021/acs.jpcc.8b05805
J. Phys. Chem. C 2018, 122, 18012−18020

dependence (Figure S4), consistent with the literature reports of equivalently oriented nanotriangles (i.e., not tilted with respect to the substrate plane).[50]

Figure 2a shows the scattering spectra of an assembled bowtie nanoantenna along with the SEM image (inset). The edge lengths of the nanotriangles are 75 and 78 nm, making this structure one of the smallest bowtie nanoantennae reported to date. Two well-resolved LSPRs are observed, one close to the wavelength of an uncoupled nanotriangle of similar size (Figure S3b), 599 nm (2.07 eV), and the other red-shifted by 294 nm (0.68 eV) to 893 nm (1.39 eV). The optical response is highly dependent upon the polarization of the incoming electric field.

The intensity of the coupled resonance mode at 893 nm is at its maximum when the electric field of the excitation light is polarized along the interparticle axis (the longitudinal axis). Rotating the polarizer by 90° (i.e., setting the polarization perpendicular to the interparticle axis) reduces the intensity of this mode to its minimum. This resonance is therefore attributed to the longitudinal coupled mode of the nanoantenna. Conversely, the mode at 599 nm is at its minimum intensity when the polarization is aligned with the interparticle axis and reaches its maximum when the polarization angle is perpendicular to the interparticle axis, consistent with the transverse mode.

A reduction in the interparticle separation for bowtie nanoantennae has been predicted to be accompanied by an increase in electric field enhancement and localization.[9] As this is also commonly linked to longitudinal mode red shifts, the energy splitting between the longitudinal and transverse modes can be thought of as an indicator for the coupling strength. The spectra of the bowtie shown in Figure 2a show an extremely large 294 nm red shift for the longitudinal mode, which suggests a strong favorable interaction, that is, an extremely strong coupling and likely high electric field localization and enhancement, consistent with the DDA simulations. The energy of the transverse mode resonance is at the same wavelength as an equivalent-sized monomer, which suggests that there is limited, if any, plasmon interaction between the two particles of the dimer for this excitation polarization.

The mode intensities vary in a sinusoidal manner with the polarizer alignment with the primary mode axes, and a 90° phase shift is apparent between the scattering intensity maxima of the two modes (Figure 2b). This is expected for the longitudinal and transverse modes within a bowtie nanoantenna and highlights that this structure has highly polarization-switchable optical properties. There is a small residual spectral contribution from the longitudinal and transverse modes when the polarizer is oriented in the transverse and longitudinal directions, respectively. This is likely to be the result of a small degree of depolarization of light through the dark-field condenser. The asymmetry toward the blue side of the longitudinal mode in Figure 2a is likely because of the longitudinal mode coupling involving one or more higher-order modes. This is supported by the observation that the spectral contribution intensity is covariant with that of the longitudinal mode, indicating the mode is aligned in the same axis.

The scattering spectra of bowtie nanoantennae were calculated using DDA. The spectra of such dimers display two spectral features with polarization-based splitting, in which a reduction in the interparticle separation causes a red shift in the longitudinal band (Figure S5). We note that these structures become increasingly more difficult to converge at very small (<2 nm) interparticle separations, except with a prohibitive number of dipoles. It is for this reason that the longitudinal mode for the simulated bowtie antenna (Figure S6a) is of higher energy than the experimental spectra.

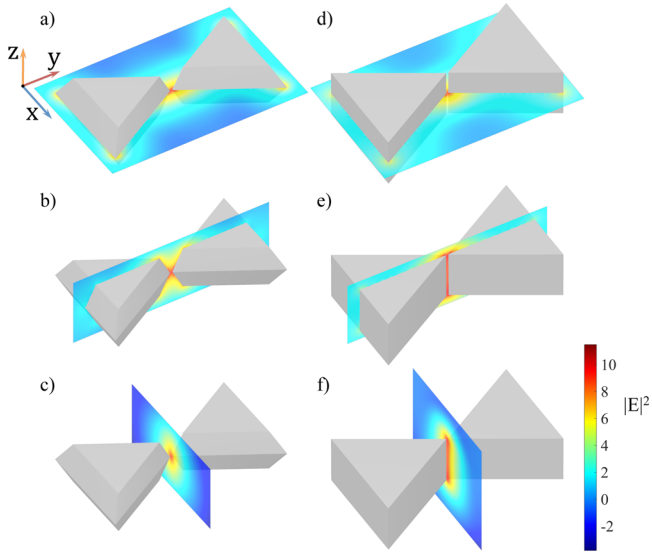

Figure 3. DDA simulated electric field intensity maps of bowties composed of nanotriangles with (a−c) chemically synthesized morphology and (d−f) triangular prism morphology. (a,d) Cross sections of the electric field intensity taken through the $x-y$ plane. (b,e) Cross sections of the electric field intensity taken through the $y-z$ plane. (c,f) Cross sections of the electric field intensity taken through the $x-z$ plane. The irradiating light for these simulations traveled parallel to the z-axis and was polarized in the direction of the y-axis. Calculation parameters were adjusted to set the edge length of each nanotriangle to 80 nm and to retain the same volume of gold per dipole, regardless of the structure geometry. The interparticle separation for the dimers in these simulations was 3 nm. The spectra for nanoantennae with chemically synthesized and plate-like morphologies are shown in Figure S6a,b.

The strong three-dimensional localization of the electric field in the interparticle space upon the assembly of these structures is shown in Figure 3 which highlights the effect of the monomer morphology in directing the field enhancement. Unlike the electric field enhancement for triangular plates (Figure 3d,f), which occurs along the full width of the plate in a line (i.e., it is confined only in the $x-y$ plane), the electric field for chemically synthesized triangles is confined in both the $x-y$ (Figure 3a) and $y-z$ planes (Figure 3c), as the nanotriangle geometry effectively leads to a bowtie-like morphology in both these planes. Consequently, the $x-z$ plane cross section taken through the interparticle space shows an electric field enhancement with a circular profile (Figure 3c). It is clear from Figure 3b,c that the nanocrystal morphology allows for three-dimensional structuring of the nanogap, reducing the extent of the electric field to a smaller volume in the interparticle space as compared to a bowtie composed of triangular prisms (Figure 3e,f).

As an additional note, the synthesized nanotriangles have aspect ratios of 2:1 (edge length/thickness). Because of this, the outermost (central) vertices are well off the surface of the supporting substrate, limiting the penetration of the electric

DOI: 10.1021/acs.jpcc.8b05805
J. Phys. Chem. C 2018, 122, 18012−18020

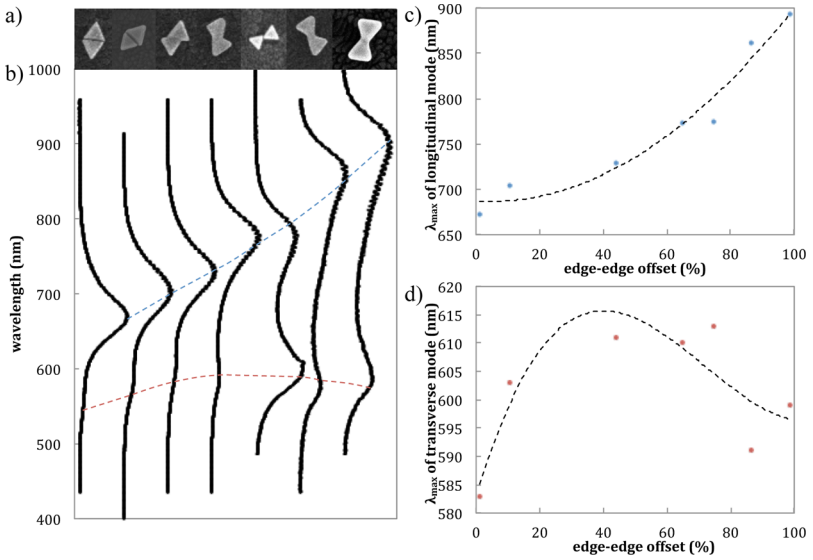

Figure 4. (a) SEM images of nanotriangle dimers (images not on the same scale) in order of increasing offset. (b) Scattering spectra of the nanotriangle dimers shown in (a), while irradiated with unpolarized white light; the longitudinal mode trend is indicated by the blue interpolation line and the transverse mode is indicated by the red interpolation line. The structures are ordered such that the offset increases monotonically; however, the spacing between the spectra is not representative of the actual offset. (c,d) Wavelengths of the (c) longitudinal and (d) transverse modes as a function of edge−edge offset percentage in the nanotriangle dimers shown in (a).

field into the substrate and, therefore, particle−substrate interactions.[50,51]

The complementary structural extreme to the bowtie antenna is an inverted bowtie, and examples are shown in Figures 2c and S7. Similar to the bowtie antenna, the scattering spectra of inverted bowties show two spectral features with a 90° phase shift between the mode maxima, indicative of the coupled longitudinal and transverse resonances (Figure 2d). However, the longitudinal mode (at a maximum when the electric field is polarized parallel to the interparticle axis) is at 704 nm (1.76 eV) for the structure shown in Figure 2c (673 nm, or 1.84 eV for Figure S7). This is much less red-shifted than that for the bowtie (105 and 74 nm shifted, respectively), whereas the transverse mode is at 603 nm (very close to that of the bowtie at 599 nm). The ratio between scattering intensities of the transverse and longitudinal modes is significantly lower for the inverted bowties than the bowtie structure, with the assembly shown in Figure S7 having a relatively lower intensity than that in Figure 2c.

The structure shown in Figure 2c is not fully symmetric and has an offset of 10% (9 nm). It is this small asymmetry that potentially allows for greater resolvability of the transverse resonance by comparison to the fully symmetric inverted bowtie in Figure S7. This is because for the inverted bowtie the transverse resonance has very low relative intensity, and the longitudinal and transverse modes are close in energy. For structures with higher offsets, more splitting between these modes occurs.

There are a number of other potential geometries for a dimer composed of two nanotriangles. In Figure 4a, we present a series of SEM images of self-assembled nanotriangle dimers (polarized scattering spectra shown in Figures S8−S11). These structures transition through increasing edge−edge offsets from an inverted bowtie (left) to a bowtie (right). Figure 4b shows the scattering spectra corresponding to the structures in Figure 4a. All structures have two spectral features, both of which transition through a range of energies as a function of edge−edge offset. These structures also have polarization-dependent optical properties and, with the exception of the inverted bowtie, well-resolved modes. The interpolation lines indicate the trends in peak position (blue for the longitudinal mode and red for the transverse mode). Figure 4c shows the trends in the peak wavelengths for the longitudinal mode as the offset varies, and this trend is replicated by DDA simulations (Figure S12b). Note that the blue shift for the longitudinal mode past 100% offset in the simulated data is a result of increasing interparticle separation which is an artifact of the requirements for simulation target generation.

Unlike the monotonic shift through 220 nm (0.45 eV) for the longitudinal mode, the shape of the transverse mode is approximately parabolic. The smaller net shift is in agreement with plasmon coupling theory[2,17,18] and the experimentally determined spectra of dimers composed of different nanoparticles (spheres,[12,14,52] nanorods,[10] and circular/ellipsoidal nanoplates[19,20]). With respect to the trend shape, the transverse mode for low offset structures is blue-shifted by comparison to a monomer and red-shifts with an increasing offset until reaching ≈50% offset, and it subsequently blue-shifts with further offset. It should be noted that the overall range for the transverse mode for these structures is 30 nm, which is on the same scale of the wavelength shifts that result from the size variance of these nanotriangles experimentally.

The transverse mode for a perfect inverted bowtie can be thought of as having a charge distribution akin to a pair of dipoles aligned in parallel, in close proximity to each other; this is energetically disfavored as these are like charges. As the offset increases, the separation between the like charges also increases, red-shifting the mode. However, with increasing offset, there is also a decrease in the coupling strength. The mode energy then can be considered a combination of transitions through two regimes: (1) A disfavored to a favored interaction, as like charges shift apart and consequently opposite charges from the opposing corners of the triangles approach. A roughly parabolic dependence upon wavelength as a function of edge−edge offset is then observed. (2) Transition from a strongly coupled to a weakly coupled interaction

DOI: 10.1021/acs.jpcc.8b05805
J. Phys. Chem. C 2018, 122, 18012−18020

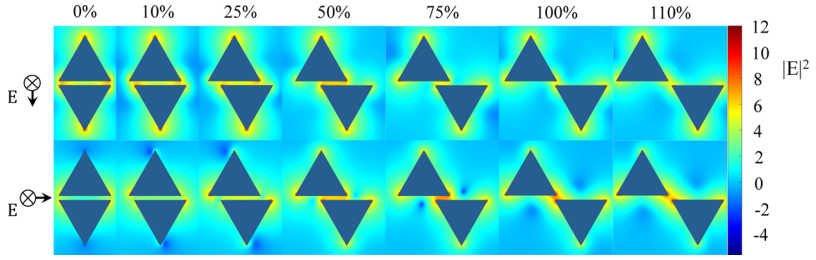

Figure 5. Simulated (DDA) electric field maps for gold nanotriangle dimers with various edge−edge offsets. Map intensity is log-scaled.

proportional to the edge−edge offset. This dictates the strength of the interaction. These effects are reflected in the simulated trends (Figure S12c), which show that the transverse mode of nanotriangle dimers shifts with respect to the offset only between 0 and 40% offset, while remaining at a static wavelength for higher offsets. Additionally, the transverse band for higher offsets appears at an equivalent wavelength to the mode of an uncoupled monomer nanotriangle. This suggests that the transverse mode is not coupled significantly strongly to affect the energy of the transverse mode from 100 to 40% offset. The blue shift from 40 to 0% offset shows that the coupling of the transverse mode is unfavorable within this offset range. Thus, for dimer structures with offsets greater than 40%, the transverse mode is characteristic of the size of the component monomers. This is reflected in Figure S13, which shows the wavelengths of the transverse modes of nanotriangle dimers with respect to the offset, normalized by the nanotriangle size (this is overlaid with the experimental transverse modes).

Figure 5 displays the effect of the offset on the electric field distribution for a series of nanotriangle dimers. For a 0% offset dimer, the electric field in the interparticle space is delocalized to a line along the contact edge of the nanoparticles, with higher intensity nodes near the vertices. As the offset increases, the two nodes shift toward each other according to the relative change of the vertex positions, eventually merging into a single, more localized and intense node concentrated primarily in the interparticle space overlap. This means an increase in the offset reduces the area over which the electric field extends. This dimer offset control combined with the effect of monomer morphology demonstrates how the electric field localization may be engineered in three dimensions.

CONCLUSIONS

The combination of the unique morphology of the chemically grown crystalline gold nanotriangles and that of the resultant dimers provides control of the electric field localization in three dimensions. Coupling between the nanocrystals arranged in a bowtie antenna results in a 294 nm red shift (0.68 eV) for the longitudinal mode. This large red shift is due to strong coupling enabled by the morphology in the interparticle region, allowing the three-dimensional localization of the electric field to the point of closest approach of the outer triangular vertices. Control over dimer geometry allows for tuning of this mode within a 220 nm (0.45 eV) range and a gradual change in the localization of the electric field. This illustrates the importance of fine morphological control of the monomer crystals to achieve strong coupling and high optical quality of the nanostructures.

ASSOCIATED CONTENT

Supporting Information

The Supporting Information is available free of charge on the ACS Publications website at DOI: 10.1021/acs.jpcc.8b05805.

UV−visible spectrum of colloid, SEM images of nanotriangle dimers, scattering spectra of monomer nanotriangles, polarized scattering spectra of nanotriangle dimers with varying offsets, DDA-simulated spectra for nanotriangle dimers with varying interparticle separations, morphologies, and offsets (PDF)

AUTHOR INFORMATION

Corresponding Author

*E-mail: alison.funston@monash.edu.

ORCID

Alison M. Funston: 0000-0002-4320-6434

Notes

The authors declare no competing financial interest.

ACKNOWLEDGMENTS

This work was supported by the Australian Research Council (ARC) Grants CE170100026 and DP140103011. The authors acknowledge the use of facilities within the Monash Centre for Electron Microscopy. This work was performed in part at the Melbourne Centre for Nanofabrication (MCN) in the Victorian Node of the Australian National Fabrication Facility (ANFF).

REFERENCES

(1) Maier, S. A. *Plasmonics: Fundamentals and Applications*; Springer US: New York, NY, 2007.

(2) Myroshnychenko, V.; Rodríguez-Fernández, J.; Pastoriza-Santos, I.; Funston, A. M.; Novo, C.; Mulvaney, P.; Liz-Marzán, L. M.; de Abajo, F. J. G. Modelling the optical response of gold nanoparticles. *Chem. Soc. Rev.* **2008**, *37*, 1792−1805.

(3) Kelly, K. L.; Coronado, E.; Zhao, L. L.; Schatz, G. C. The Optical Properties of Metal Nanoparticles: The Influence of Size, Shape, and Dielectric Environment. *J. Phys. Chem. B* **2003**, *107*, 668−677.

(4) Duan, H.; Fernández-Domínguez, A. I.; Bosman, M.; Maier, S. A.; Yang, J. K. W. Nanoplasmonics: Classical down to the Nanometer Scale. *Nano Lett.* **2012**, *12*, 1683−1689.

(5) Wiener, A.; Duan, H.; Bosman, M.; Horsfield, A. P.; Pendry, J. B.; Yang, J. K. W.; Maier, S. A.; Fernández-Domínguez, A. I. Electron-Energy Loss Study of Nonlocal Effects in Connected Plasmonic Nanoprisms. *ACS Nano* **2013**, *7*, 6287−6296.

(6) Huang, J.-S.; Callegari, V.; Geisler, P.; Brüning, C.; Kern, J.; Prangsma, J. C.; Wu, X.; Feichtner, T.; Ziegler, J.; Weinmann, P.; et al. Atomically flat single-crystalline gold nanostructures for plasmonic nanocircuitry. *Nat. Commun.* **2010**, *1*, 150.

(7) Sánchez-Iglesias, A.; Pastoriza-Santos, I.; Pérez-Juste, J.; Rodríguez-González, B.; de Abajo, F. J. G.; Liz-Marzán, L. M.

Synthesis and Optical Properties of Gold Nanodecahedra with Size Control. *Adv. Mater.* **2006**, *18*, 2529−2534.
(8) Rodríguez-Lorenzo, L.; Alvarez-Puebla, R. A.; Pastoriza-Santos, I.; Mazzucco, S.; Stéphan, O.; Kociak, M.; Liz-Marzán, L. M.; de Abajo, F. J. G. Zeptomol Detection Through Controlled Ultrasensitive Surface-Enhanced Raman Scattering. *J. Am. Chem. Soc.* **2009**, *131*, 4616−4618.
(9) Dodson, S.; Haggui, M.; Bachelot, R.; Plain, J.; Li, S.; Xiong, Q. Optimizing Electromagnetic Hotspots in Plasmonic Bowtie Nanoantennae. *J. Phys. Chem. Lett.* **2013**, *4*, 496−501.
(10) Funston, A. M.; Novo, C.; Davis, T. J.; Mulvaney, P. Plasmon Coupling of Gold Nanorods at Short Distances and in Different Geometries. *Nano Lett.* **2009**, *9*, 1651−1658.
(11) Romero, I.; Aizpurua, J.; Bryant, G. W.; De Abajo, F. J. G. Plasmons in nearly touching metallic nanoparticles: singular response in the limit of touching dimers. *Opt. Express* **2006**, *14*, 9988−9999.
(12) Barrow, S. J.; Funston, A. M.; Gómez, D. E.; Davis, T. J.; Mulvaney, P. Surface Plasmon Resonances in Strongly Coupled Gold Nanosphere Chains from Monomer to Hexamer. *Nano Lett.* **2011**, *11*, 4180−4187.
(13) Barrow, S. J.; Wei, X.; Baldauf, J. S.; Funston, A. M.; Mulvaney, P. The surface plasmon modes of self-assembled gold nanocrystals. *Nat. Commun.* **2012**, *3*, 1275.
(14) Barrow, S. J.; Funston, A. M.; Wei, X.; Mulvaney, P. DNA-directed self-assembly and optical properties of discrete 1D, 2D and 3D plasmonic structures. *Nano Today* **2013**, *8*, 138−167.
(15) Fan, J. A.; Wu, C.; Bao, K.; Bao, J.; Bardhan, R.; Halas, N. J.; Manoharan, V. N.; Nordlander, P.; Shvets, G.; Capasso, F. Self-Assembled Plasmonic Nanoparticle Clusters. *Science* **2010**, *328*, 1135−1138.
(16) Zuloaga, J.; Prodan, E.; Nordlander, P. Quantum Description of the Plasmon Resonances of a Nanoparticle Dimer. *Nano Lett.* **2009**, *9*, 887−891.
(17) Prodan, E.; Nordlander, P. Plasmon hybridization in spherical nanoparticles. *J. Chem. Phys.* **2004**, *120*, 5444−5454.
(18) Prodan, E. A Hybridization Model for the Plasmon Response of Complex Nanostructures. *Science* **2003**, *302*, 419−422.
(19) Huang, W.; Qian, W.; Jain, P. K.; El-Sayed, M. A. The Effect of Plasmon Field on the Coherent Lattice Phonon Oscillation in Electron-Beam Fabricated Gold Nanoparticle Pairs. *Nano Lett.* **2007**, *7*, 3227−3234.
(20) Gunnarsson, L.; Rindzevicius, T.; Prikulis, J.; Kasemo, B.; Käll, M.; Zou, S.; Schatz, G. C. Confined Plasmons in Nanofabricated Single Silver Particle Pairs: Experimental Observations of Strong Interparticle Interactions. *J. Phys. Chem. B* **2005**, *109*, 1079−1087.
(21) Kotkowiak, M.; Grześkiewicz, B.; Robak, E.; Wolarz, E. Interaction between Nanoprisms with Different Coupling Strength. *J. Phys. Chem. C* **2015**, *119*, 6195−6203.
(22) Marinica, D. C.; Kazansky, A. K.; Nordlander, P.; Aizpurua, J.; Borisov, A. G. Quantum Plasmonics: Nonlinear Effects in the Field Enhancement of a Plasmonic Nanoparticle Dimer. *Nano Lett.* **2012**, *12*, 1333−1339.
(23) Rosen, D. A.; Tao, A. R. Modeling the Optical Properties of Bowtie Antenna Generated By Self-Assembled Ag Triangular Nanoprisms. *ACS Appl. Mater. Interfaces* **2014**, *6*, 4134−4142.
(24) Bi, G.; Wang, L.; Ling, L.; Yokota, Y.; Nishijima, Y.; Ueno, K.; Misawa, H.; Qiu, J. Optical properties of gold nano-bowtie structures. *Opt. Commun.* **2013**, *294*, 213−217.
(25) Li, G.; Chen, X.; Huang, L.; Wang, J.; Hu, W.; Lu, W. The localized near-field enhancement of metallic periodic bowtie structure: An oscillating dipoles picture. *Phys. B* **2012**, *407*, 2223−2228.
(26) Schraml, K.; Spiegl, M.; Kammerlocher, M.; Bracher, G.; Bartl, J.; Campbell, T.; Finley, J. J.; Kaniber, M. Optical properties and interparticle coupling of plasmonic bowtie nanoantennas on a semiconducting substrate. *Phys. Rev. B: Condens. Matter Mater. Phys.* **2014**, *90*, 035435.
(27) Kaniber, M.; Schraml, K.; Regler, A.; Bartl, J.; Glashagen, G.; Flassig, F.; Wierzbowski, J.; Finley, J. J. Surface plasmon resonance spectroscopy of single bowtie nano-antennas using a differential reflectivity method. *Sci. Rep.* **2016**, *6*, 23203.
(28) Chien, M.-H.; Nien, L.-W.; Chao, B.-K.; Li, J.-H.; Hsueh, C.-H. Effects of the rotation angle on surface plasmon coupling of nanoprisms. *Nanoscale* **2016**, *8*, 3660−3670.
(29) Chao, B.-K.; Lin, S.-C.; Nien, L.-W.; Li, J.-H.; Hsueh, C.-H. Effects of corner radius on periodic nanoantenna for surface-enhanced Raman spectroscopy. *J. Opt.* **2015**, *17*, 125002.
(30) Aldaye, F. A.; Sleiman, H. F. Sequential Self-Assembly of a DNA Hexagon as a Template for the Organization of Gold Nanoparticles. *Angew. Chem., Int. Ed.* **2006**, *45*, 2204−2209.
(31) Fan, J. A.; He, Y.; Bao, K.; Wu, C.; Bao, J.; Schade, N. B.; Manoharan, V. N.; Shvets, G.; Nordlander, P.; Liu, D. R.; et al. DNA-Enabled Self-Assembly of Plasmonic Nanoclusters. *Nano Lett.* **2011**, *11*, 4859−4864.
(32) Lalander, C. H.; Zheng, Y.; Dhuey, S.; Cabrini, S.; Bach, U. DNA-directed self-assembly of gold nanoparticles onto nanopatterned surfaces: Controlled placement of individual nanoparticles into regular arrays. *ACS Nano* **2010**, *4*, 6153−6161.
(33) Lermusiaux, L.; Sereda, A.; Portier, B.; Larquet, E.; Bidault, S. Reversible Switching of the Interparticle Distance in DNA-Templated Gold Nanoparticle Dimers. *ACS Nano* **2012**, *6*, 10992−10998.
(34) Mastroianni, A. J.; Claridge, S. A.; Alivisatos, A. P. Pyramidal and Chiral Groupings of Gold Nanocrystals Assembled Using DNA Scaffolds. *J. Am. Chem. Soc.* **2009**, *131*, 8455−8459.
(35) Yao, H.; Yi, C.; Tzang, C.-H.; Zhu, J.; Yang, M. DNA-directed self-assembly of gold nanoparticles into binary and ternary nanostructures. *Nanotechnology* **2007**, *18*, 015102.
(36) Novo, C.; Funston, A. M.; Pastoriza-Santos, I.; Liz-Marzán, L. M.; Mulvaney, P. Spectroscopy and High-Resolution Microscopy of Single Nanocrystals by a Focused Ion Beam Registration Method. *Angew. Chem., Int. Ed.* **2007**, *46*, 3517−3520.
(37) Draine, B. T.; Flatau, P. J. Discrete-Dipole Approximation For Scattering Calculations. *J. Opt. Soc. Am. A* **1994**, *11*, 1491−1499.
(38) Draine, B. T.; Flatau, P. J. *User Guide for the Discrete Dipole Approximation Code DDSCAT 7.1*, 2010.
(39) Koch, E.-E.; Krakfa, C.; Lynch, D. W.; Weaver, J. H. *Optical Properties of Metals: Noble Metals, Aluminium, Scandium, Yttrium, the Lanthanides and the Actinides*; Fachinformationszentrum Energie: Karlsruhe, 1981.
(40) Novo, C.; Funston, A. M.; Pastoriza-Santos, I.; Liz-Marzán, L. M.; Mulvaney, P. Influence of the Medium Refractive Index on the Optical Properties of Single Gold Triangular Prisms on a Substrate. *J. Phys. Chem. C* **2008**, *112*, 3−7.
(41) Vernon, K. C.; Funston, A. M.; Novo, C.; Gómez, D. E.; Mulvaney, P.; Davis, T. J. Influence of Particle−Substrate Interaction on Localized Plasmon Resonances. *Nano Lett.* **2010**, *10*, 2080−2086.
(42) Scarabelli, L.; Coronado-Puchau, M.; Giner-Casares, J. J.; Langer, J.; Liz-Marzán, L. M. Monodisperse gold nanotriangles: Size control, large-scale self-assembly, and performance in surface-enhanced raman scattering. *ACS Nano* **2014**, *8*, 5833−5842.
(43) Chen, L.; Ji, F.; Xu, Y.; He, L.; Mi, Y.; Bao, F.; Sun, B.; Zhang, X.; Zhang, Q. High-Yield Seedless Synthesis of Triangular Gold Nanoplates through Oxidative Etching. *Nano Lett.* **2014**, *14*, 7201−7206.
(44) Rodríguez-Lorenzo, L.; Álvarez-Puebla, R. A.; de Abajo, F. J. G.; Liz-Marzán, L. M. Surface Enhanced Raman Scattering Using Star-Shaped Gold Colloidal Nanoparticles. *J. Phys. Chem. C* **2010**, *114*, 7336−7340.
(45) Hirai, H.; Yakura, N. Protecting polymers in suspension of metal nanoparticles. *Polym. Adv. Technol.* **2001**, *12*, 724−733.
(46) Louie, S. M.; Gorham, J. M.; Tan, J.; Hackley, V. A. Ultraviolet photo-oxidation of polyvinylpyrrolidone (PVP) coatings on gold nanoparticles. *Environ. Sci.: Nano* **2017**, *4*, 1866−1875.
(47) Koczkur, K. M.; Mourdikoudis, S.; Polavarapu, L.; Skrabalak, S. E. Polyvinylpyrrolidone (PVP) in nanoparticle synthesis. *Dalton Trans.* **2015**, *44*, 17883−17905.
(48) Barrow, S. J.; Rossouw, D.; Funston, A. M.; Botton, G. A.; Mulvaney, P. Mapping Bright and Dark Modes in Gold Nanoparticle

DOI: 10.1021/acs.jpcc.8b05805
J. Phys. Chem. C 2018, 122, 18012−18020

Chains using Electron Energy Loss Spectroscopy. *Nano Lett.* **2014**, *14*, 3799−3808.
(49) Atay, T.; Song, J.-H.; Nurmikko, A. V. Strongly Interacting Plasmon Nanoparticle Pairs: From Dipole−Dipole Interaction to Conductively Coupled Regime. *Nano Lett.* **2004**, *4*, 1627−1631.
(50) Smith, K. W.; Yang, J.; Hernandez, T.; Swearer, D. F.; Scarabelli, L.; Zhang, H.; Zhao, H.; Moringo, N. A.; Chang, W.-S.; Liz-Marzán, L. M.; et al. Environmental Symmetry Breaking Promotes Plasmon Mode Splitting in Gold Nanotriangles. *J. Phys. Chem. C* **2018**, *122*, 13259−13266.
(51) Knight, M. W.; Wu, Y.; Lassiter, J. B.; Nordlander, P.; Halas, N. J. Substrates Matter: Influence of an Adjacent Dielectric on an Individual Plasmonic Nanoparticle. *Nano Lett.* **2009**, *9*, 2188−2192.
(52) Sheikholeslami, S.; Jun, Y.-w.; Jain, P. K.; Alivisatos, A. P. Coupling of optical resonances in a compositionally asymmetric plasmonic nanoparticle dimer. *Nano Lett.* **2010**, *10*, 2655−2660.

DOI: 10.1021/acs.jpcc.8b05805
J. Phys. Chem. C 2018, 122, 18012−18020